Non-linear dynamics of semi-dilute polydisperse polymer solutions in microfluidics: A study of a benchmark flow problem

Zhuo Li [a], Xue-Feng Yuan [a,*], Simon J. Haward [b], Jeffrey A. Odell [b], Stephen Yeates [c]

[a] Manchester Interdisciplinary Biocentre, School of Chemical Engineering and Analytical Science, The University of Manchester, 131 Princess Street, Manchester M1 7DN, UK
[b] HH Wills Physics Laboratory, The University of Bristol, Tyndall Avenue, Bristol BS8 1TL, UK
[c] School of Chemistry, The University of Manchester, Oxford Road, Manchester, M13 9PL, UK

ARTICLE INFO

ABSTRACT

The complex flow behaviour of semi-dilute ($15 < c/c^* < 22.5$) polydisperse polyethylene oxide (PEO) aqueous solutions flowing through a planar microfluidic geometry with an 8:1:8 contraction–expansion is systematically studied. The molecular weight and distribution of the PEO samples are analysed by Gel Permeation Chromatography (GPC). Full rheometric characterizations using various techniques including piezoelectric axial vibrator (PAV) measurements at frequencies as high as 6700 Hz are carried out for one semi-dilute PEO solution. Complex flows over a wide range of elasticity numbers ($20 \leqslant El \leqslant 120$), Weissenberg numbers ($7 \leqslant Wi \leqslant 121$) and Reynolds numbers ($0.08 \leqslant Re \leqslant 4.5$) are characterized using micro-particle image velocimetry (μ-PIV) and pressure drop measurements. The evolution of vortex formation and dynamics has been visualized through a step-flow-rate experiment. The effect of El on vortex stability has been studied. Various flow dynamics regimes have been quantified and are presented in a Wi–Re diagram. The experimental results reveal that the elastic behaviour of polymer solutions is very sensitive to high molecular weight polymer in the polydisperse polymer samples, and the contraction ratio and the aspect ratio of flow geometry are the important design parameters in controlling the non-linear dynamics of semi-dilute polymer solutions in microfluidics.

1. Introduction

Studying the non-linear dynamics of polymer solutions in microfluidic devices is of great significance to the design and optimization of many industrial applications, such as oil recovery, high-speed electro-spraying, electro-spinning and inkjet printing, which exhibit highly nonlinear flow phenomena. James and Saringer [1] demonstrated that the viscoelastic properties of dilute polymer solutions can be enhanced by reducing contraction geometry scales down to the micrometer scale. Groisman et al. [2] used a micro-fabricated rectifier to reveal some unusual rheological behaviour of polymer solution. The deformation of a single DNA molecule in microfluidics has been studied in shear flow [3–5], elongational flow [6,7], and mixed flow [8]. In many cases, this rapidly evolving area provides enormous opportunities for better understanding the fundamental physics of viscoelastic fluid flow. By reducing the flow geometry to a much smaller size, very high deformation rates can be readily realized in microfluidics, with minimum inertial effects [9–15]. It thus provides access to the high Weissenberg number (Wi) and moderate Reynolds number (Re) flow regimes [9,10,14,15], in which elastic forces dominate. Hence, even low viscosity polymer solutions can exhibit very strong viscoelastic flow behaviour.

Numerous researchers have studied the dynamics of non-Newtonian fluids in macroscopic contraction flow experimentally [16–26] and numerically [27–32]. These studies mainly focused on the effects of the rheological properties of fluids, the contraction ratio (β), the sharpness of the re-entrant corner and the flow rate on the flow patterns at different flow regimes, the mechanism of vortex evolution, the excess pressure drop over Newtonian fluids and the interplay between inertia and elasticity. There have been several comprehensive reviews on macroscale entry flow in the literature [9,33,34].

In contrast to macroscale geometries, Rodd et al. [9,10] experimentally studied the inertial-elastic interaction in flow of polymer solutions through a micro-planar geometry with 16:1:16 contraction–expansion. Flow characterizations were carried out over a range of elasticity numbers, $El = Wi/Re$. A Wi–Re diagram was constructed to classify the different flow regimes, including Newtonian-like, inertial-elastic instability and vortex growth, along a fixed El which represents the trajectory of a set of experiments with a given viscoelastic fluid and flow geometry. Gulati et al. [14] has investigated the flow of a semi-dilute DNA solution through a micro-fabricated planar geometry with a contraction ratio of 2:1, under high Wi ($0.8 < Wi < 629$) and negligible Re

* Corresponding author. Tel.: +44 (0) 161 306 4887; fax: +44 (0) 161 306 5201.
E-mail address: xue-feng.yuan@manchester.ac.uk (X.-F. Yuan).

$(6.0 \times 10^{-7} < Re < 9.8 \times 10^{-2})$, thereby achieving very high El $(1.4 \times 10^3 < El < 1.4 \times 10^6)$. Steady and symmetric growth of the corner vortex was observed over a wide range of Wi in this work, in contrast to that of Rodd et al [9,10]. In our recent experimental work [15], we studied the flow of thermodynamically ideal solutions of a high molecular weight atactic polystyrene (aPS) in dioctyl phthalate (DOP) through a planar micro-contraction with contraction ratio 8:1. The channel provided a high aspect ratio of 16:1 and a good approximation to 2D flow in the narrow downstream channel. Both birefringence and μ-PIV were used to assess the macromolecular strain in the entry region and to characterize the flow patterns in the upstream channel.

The pressure drop across the contraction is an important quantity to characterize the non-linear dynamics of viscoelastic fluids in planar entry flows. Earlier macroscale experiments in axisymmetric contractions showed a substantial extra pressure drop, well above the value measured for a Newtonian fluid with the same viscosity [20,21,35]. However only a few experimental and numerical studies have considered the pressure drop in macroscale *planar* contraction flow [26,28]. An increased pressure drop was also found in microscale experiments [1,2,9,10,14]. Groisman et al. [2] quantify the non-linear behaviour of polymer solutions in a microfluidic flow rectifier by plotting the total flow resistance (pressure drop) against flow rate. The extra pressure drop is attributed to the unravelling [36] of polymer molecules when the extension rate is sufficiently large compared to the reciprocal relaxation time. The results of Rodd et al. [10] showed that the enhancement of pressure drop is associated with the onset of elastic instability. Pressure drop was also measured in [15] to evaluate the non-Newtonian viscosity, and transitions in the flow pattern are reflected by transitions in the relative viscosity and the macromolecular strain determined from birefringence measurements.

There are obvious differences between the flow patterns observed by Rodd et al. [9,10] with contraction–expansion ratio 16:1:16, and by Gulati et al. [14] with contraction ratio 2:1. Apart from the different El, contraction ratio and length of the downstream narrow channel, the polydispersity and flexibility of chain molecules could play important roles in the upstream vortex dynamics. In the present paper, we report the non-linear dynamics of semi-dilute polydisperse polymer aqueous solutions in a planar microfluidic geometry with an 8:1:8 contraction–expansion ratio. In Section 2, the molecular characterization of polydisperse polyethylene oxide (PEO) samples and the preparation of a series of PEO solutions are presented, along with experimental techniques, including the details of the micro-channel geometry, rheometry, μ-PIV and pressure measurements. The results and discussion of rheometric and flow characterizations over a wide range of El $(20 \leqslant El \leqslant 120)$, Wi $(7 \leqslant Wi \leqslant 121)$ and Re $(0.08 \leqslant Re \leqslant 4.5)$ follow in Section 3. The effect of the polydispersity of polymers on their extensional viscosity is highlighted. Various flow regimes along El lines are classified in a Wi–Re diagram. The evolution of flow patterns are analysed and correlated with the pressure drop measurements. Conclusions are given in Section 4.

2. Preparation of PEO solutions and experimental techniques

2.1. Molecular characterization and preparation of PEO solutions

The molecular weights and molecular weight distributions of two PEO samples were characterized using standard GPC with TSK PW 5000 and 6000 columns, an ERC 751A differential refractometer and a Waters 510 pump, and an aqueous solvent. PEO(I) is a pharmaceutical grade sample (POLYOX™ WSR N-60K) kindly supplied by Dow Chemicals. PEO(II) is a research grade sample (Polymer Standard, Batch No.: 20842-9) from Polymer Laborato-
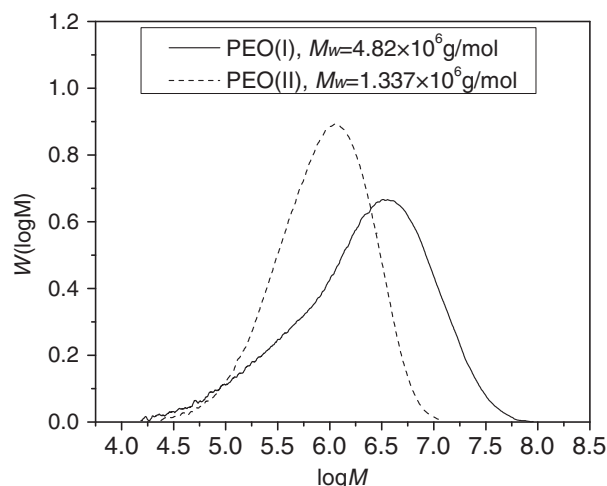

Fig. 1. Molecular weight distributions of PEO(I) and PEO(II) measured by GPC.

Table 1
Molecular characterization.

	$10^{-5}M_n$	$10^{-6}M_w$	$10^{-6}M_z$	M_w/M_n	M_z/M_w	R_g (nm)	c^* (wt.%)
PEO(I)	6.40	4.82	14.1	7.50	2.90	169	0.0206
PEO(II)	0.47	1.34	2.62	2.82	1.93	80.3	0.0538

ries. The GPC results are shown in Fig. 1 and Table 1. Note that the PEO(II) was labelled by Polymer Laboratories as $M_w = 1.34 \times 10^6$ g/mol and $M_w/M_n = 1.13$. The significant discrepancy in the polydispersity of PEO(II) probably results from the use of different GPC columns. In the present work, the pore size of a gel in the GPC columns were carefully tuned in order to resolve more accurately the molecular weight distribution of PEO. The data presented in Fig. 1 and Table 1 is significant in quantifying the difference between the PEO(I) and PEO(II) samples under the same GPC and analytical procedure. The mean radius of gyration (R_g) of PEO molecules was estimated from $\langle R_g \rangle = 0.215 M_w^{0.583 \pm 0.031}$ (Å) proposed by Devanand and Selser [37]. The overlap concentrations c^* are calculated by assuming a simple cubic packing of PEO molecules, i.e. $c^* = M_w/[N_A(2R_g)^3]$ (N_A is Avogadro's constant). The results of the molecular characterization are listed in Table 1. Note that the estimation of the c^* value based on the simple cubic packing assumption is about half of the value estimated by Rodd et al. [9] who used the closest sphere packing assumption.

A series of semi-dilute PEO(I) and PEO(II) aqueous solutions with concentrations up to $c/c^* = 22.5$ were prepared by dissolving PEO powder in de-ionized water. The solutions were stored in a refrigerator at 4 °C for about 7 days, with occasional and gentle shaking by hand to allow complete dissolution of PEO whilst avoiding mechanical degradation. Only freshly made PEO aqueous solutions were used in each experiment reported hereafter.

2.2. Rheometry

The rheometric properties of the PEO solutions were measured using a range of experimental techniques. The apparatus included an ARES rotational shear rheometer (TA Instruments) with a double wall Couette geometry (cup OD = 34 mm, cup ID = 27.95 mm, bob OD = 32 mm, bob ID = 29.5 mm), a novel Piezo-Axial-Vibrator (IDM-PAV) (The Institute for Dynamic Materials Testing, Germany) and a CaBER capillary breakup extensional rheometer (Thermo Fisher Scientific). As demonstrated by Crassous et al. [38],
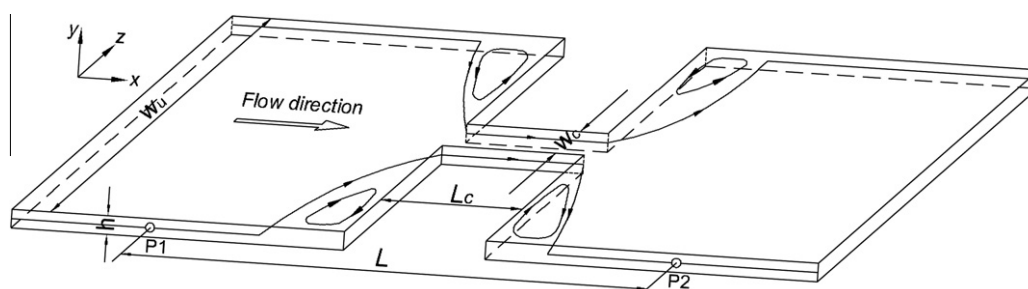
Fig. 2. Schematic diagram of the 8:1:8 abrupt planar contraction geometry including definitions of important length scales. The entrance of the contraction throat is located as the origin ($x = 0$, $y = 0$, $z = 0$).

Table 2
Microchannel geometries.

w_u (μm)	w_c (μm)	L (mm)	L_c (mm)	h (μm)	D_h (μm)	β	α	ε_H
800	102	40.000	20.000	45	62	8:1:8	9/160	2.1

IDM-PAV can measure the storage modulus G' and the loss modulus G'' of complex fluids over a much wider frequency range than conventional rheometers. The characteristic relaxation time (λ) and surface tension (κ) of all the PEO(I) and PEO(II) solutions were measured using CaBER and CIR100 Interfacial Rheometers (Camtel Ltd.), respectively.

2.3. Micro-channel geometry

The microfluidic chip is made of poly(methyl methacrylate) (PMMA) and aromatic epoxy, fabricated by standard soft lithographic method (Epigem Ltd., the UK). Fig. 2 shows a schematic diagram. Its geometric details are listed in Table 2, including the width (w_u) of the upstream channel, the width (w_c) and length (L_c) of the narrow channel, the uniform depth (h) of the channels, the hydraulic diameter of the narrow channel D_h ($D_h = 2w_c h/(w_c + h)$), the contraction–expansion ratio β ($\beta = w_u/w_c$), the aspect ratio α ($\alpha = h/w_u$) and the total Hencky strain ε_H experienced by a fluid element. The Hencky strain is estimated by $\varepsilon_H = ln(w_u/w_c)$. In contrast to other micro-channels reported in the literatures, the length of the narrow channel ($L_c = 20$ mm) is about 200 times its width. This ensures that the fluid flow in the narrow channel is fully developed and that the downstream non-linear flow in the expansion region has minimal effects on the upstream vortex dynamics. A syringe pump (Harvard Apparatus Ultra-High Pressure PHD 2000) was used to drive fluid flow to achieve a range of volumetric flow rates (e.g. 0.5 ml/h $\leqslant Q \leqslant$ 50 ml/h for de-ionized water).

2.4. Micro-particle image velocimetry

Velocity fields at the centre-plane of the flow channel were measured using a micro-particle image velocimeter (TSI Instrument Ltd.). This consists of three modules: a pulsed Nd:YAG laser with 532nm wavelength, a microscope (Nikon TE2000-E) with fluorescent filter and a CCD camera (1280 × 1024 × 12 bits, 8 Hz). Standard Nikon 10× objective lens ($NA = 0.3$) and 20× objective lens ($NA = 0.45$) were used. PEO solutions were seeded with 0.01 wt.% Epi-fluorescent particles (diameter $d_p = 1.0$ μm, $Ex_{max.}/Em_{max.} = 542/612$ nm). The fluorescent particles absorb the illuminating laser beam (∼532 nm) and emit light with a longer wavelength (∼560 nm). The details of the μ-PIV technique can be found in [39,40].

For the above μ-PIV system setting, the estimated measurement depth is 26 μm if using 10× ($NA = 0.3$) lens or 12 μm if using 20× ($NA = 0.45$) lens [41]. These depths of field are equivalent to 58% or 27% of the channel depth ($h = 45$ μm), respectively. Particle images under a given flow condition were captured in sequence, and then analysed using the cross-correlation PIV algorithm and Nyquist criterion (TSI Insight3G software) with an interrogation area of 48 × 48 pixels. The error in the velocity measurements is about 12–16% below the true value. This systematic error could be reduced were a higher magnification objective lens with a larger NA used.

2.5. Pressure drop measurement

Pressure sensors (Linkam Scientific Instrument Ltd.) were carefully calibrated over their entire working range by applying a series of known pressures. The sensors were deployed at the positions P1 and P2 (see Fig. 2), to measure the overall pressure drop ΔP_{12} across the contraction–expansion flow. In addition, in order to characterize the fully developed flow in straight narrow channel, the pressure drop was measured across the 20 mm middle section
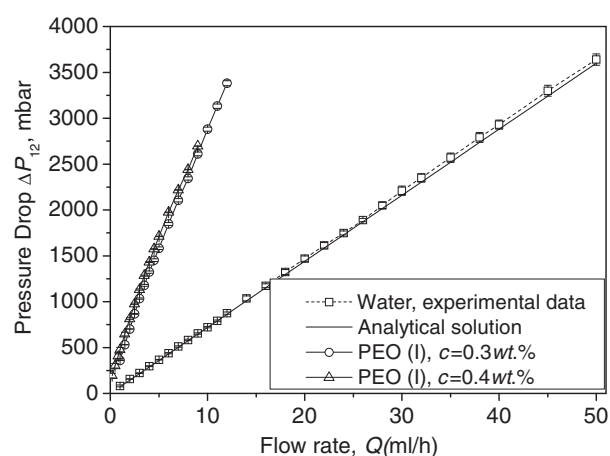

Fig. 3. Pressure drop (ΔP_{12}) vs. flow rate for de-ionized water, 0.3 and 0.4 wt.% PEO(I) solutions flowing through the 20 mm straight microchannel with rectangular cross-section 102 μm (width) × 45μm (depth), respectively, and a comparison of the pressure drop of de-ionized water between experiment values and analytical solution.

of a 40 mm straight rectangular channel of dimension $w_c \times h$. The distance between the location of the pressure sensors and the in-let/outlet plane or the contraction/expansion plane is no less than 10 mm to avoid the effects of transient flow and the presence of the upstream and downstream vortex. The pressure drop of either de-ionized water or PEO solutions was measured over a range of flow rates. Data acquisition was taken by using a Bluechip PCI ADC card and in-house software.

The steady state pressure drop for the fully developed flow of water between the two ends of the 20 mm straight channel with a rectangular cross-section of width 102 μm and depth 45 μm is plotted against flow rate in Fig. 3. The results are in excellent agreement with analytical solutions [42], with less than 1% errors. The pressure drops of 0.3 and 0.4 wt.% PEO(I) through the same flow channel at various flow rates will be used for the extraction of the excess pressure drop as presented in Section 3.8.

3. Results and discussion

3.1. Relaxation time and extensional viscosity

Fig. 4 displays the decay of the mid-filament diameter with time from CaBER measurements, approximating to a single exponential. The effective relaxation time can be extracted by fitting the experimental curves [43]. The slower the decay rate of a filament the longer is its relaxation time. Unlike the PEO(I) solutions, the PEO(II)
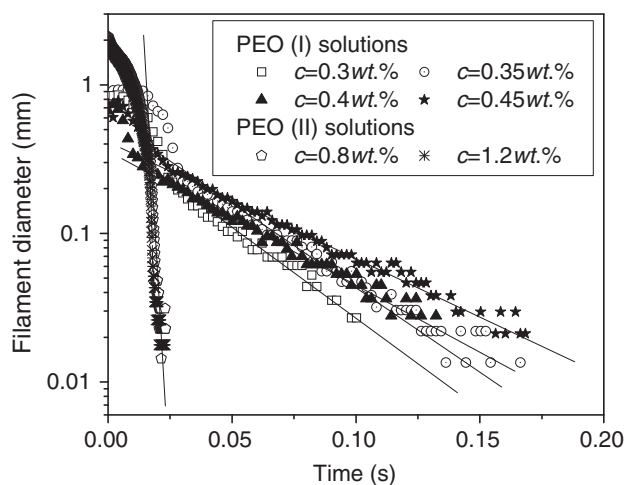

Fig. 4. Transient mid-filament diameter of PEO(I) and PEO(II) aqueous solutions decay with time. The data were obtained from measurements of *CaBER* extensional rheometer using the following geometries: h_0 = 4mm, h_f = 10.08 mm, R_0 = 2 mm for 0.3 wt.% PEO(I); h_0 = 4 mm, h_f = 10.35 mm, R_0 = 2 mm for 0.35 wt.% PEO(I); h_0 = 4 mm, h_f = 10.59 mm, R_0 = 2 mm for 0.4 wt.% PEO(I); h_0 = 4 mm, h_f = 11.03 mm, R_0 = 2 mm for 0.45 wt.% PEO(I); h_0 = 4 mm, h_f = 6 mm and R_0 = 2 mm for 0.8 and 1.2 wt.% PEO(II), respectively.

solutions do not show significant elastic fluid characteristics, even at a concentration as high as c/c^* = 22.3 or 1.2 wt.%. The extremely high molecular weight PEO(I) molecules in the tail of its molecular weight distribution play a very important role in the elastic fluid behaviour of semi-dilute PEO(I) solutions. Therefore only PEO(I) solutions will be studied hereafter. The surface tension and relaxation time of four semi-dilute PEO(I) solutions are listed in Table 3. The relaxation time of polymer solutions increases with the polymer concentration. All dimensionless numbers Re, Wi and El used in the flow experiments are also presented in Table 3.

The relaxation time of 0.3 wt.% PEO(I) solution measured by Ca-BER is in a reasonable agreement with that obtained using a cross-slot extensional rheometer [44]. The cross-slot rheometer measures the excess pressure drop over the cross-slot for estimation of the extensional viscosity of complex fluids. The "steady state" extensional viscosity measured by this device is in a sense that under a given deformational rate the excess pressure drop reaches its steady state. The extensional viscosity for 0.3 wt.% PEO(I) solution obtained by this technique is plotted against the extensional rate in Fig. 5. The extensional viscosity shows a rapid increase to a peak of about 27 Pa s at an extensional rate of 80 s^{-1}. Beyond $\dot{\varepsilon}$ = 80 s^{-1}, the apparent reduction of the extensional viscosity is explained by flow perturbation [44]. The measurement protocol and the technical details can be found from [44,45].

3.2. Relaxation spectrum and steady shear viscosity

The linear viscoelastic response region of the 0.3 wt.% PEO(I) solution was determined by the dynamic strain sweep test at 1 Hz using ARES rheometer. Within its linear response region (small strain <0.4), the dynamic frequency sweep tests were carried out by ARES at the strain of 0.2 and by IDM-PAV at the strain of 0.0004, respectively. The complementary G' and G'' data for the 0.3 wt.% PEO(I) solution are overlaid in Fig. 6a. Note that ARES cannot access very low frequency ranges due to the high noise level in measurements with low viscosity fluids, and also that significant inertial effects in the ARES data start at a frequency of around 10 Hz.

The zero-shear viscosities of the four semi-dilute PEO(I) solutions are listed in Table 3. Their shear viscosities at 25 °C are plotted against shear rate in Fig. 6b. They are shear-thinning fluids. For higher shear rates (>2000 s^{-1}), inertial effects become significant and the data from the ARES rheometer becomes unreliable.

3.3. Evolution of vortex dynamics

In order to uncover the evolution of vortex formation and dynamics in 0.3 wt.% PEO(I) solution in 8:1 contraction flow, μ-PIV was used to capture images of the flow pattern over a period of 5.25 s after a step change (at time t = 0) in the flow rate from Q = 3.5 ml/h (Re = 1.25, Wi = 24.9) to Q = 4.5ml/h (Re = 1.6, Wi = 32.0), as shown in Fig. 7.

Table 3
Properties of PEO(I) aqueous solutions at 25 °C and a range of flow dimensionless numbers.

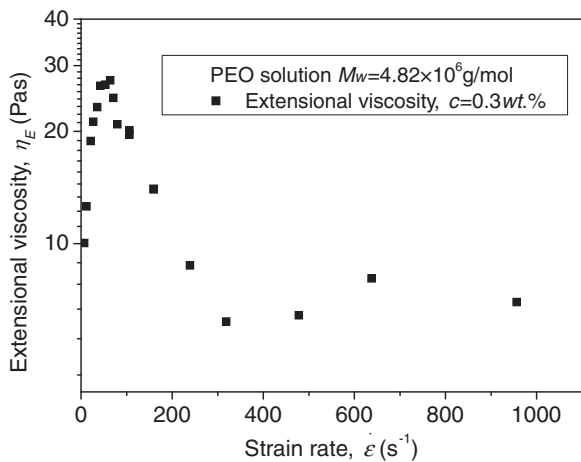| c (wt%)	0.3	0.35	0.4	0.45
ρ (kg/m^3)	991	990	989	988
c/c^*	15	17.5	20	22.5
η_0 (mPa s)	10.5	13.5	17.5	22.5
κ (mN/M)	60.7	60	58.8	58.4
λ_{CaBER} (ms)	6	9	13	17
$\dot{\gamma} = 2\langle V_c\rangle/w_c$ (1/s)	1186–14,232	1186–9488	1186–8302	593–7116
$Re = \rho\overline{V_c}D_h/\eta_0 = 2\rho Q/(w_c + h)\eta_0$	0.36–4.3	0.28–2.2	0.21–1.6	0.08–1.0
$Wi = \lambda\dot{\gamma}_c = 2\lambda\overline{V_c}/w_c = 2\lambda Q/hw_c^2$	7.1–85.4	10.7–85.4	15.4–108	10.1–121
$El = Wi/Re = \lambda\eta(w_c + h)/\rho w_c^2 h$	20	38	71	120

Fig. 5. Extensional viscosity of 0.3 wt.% PEO(I) solution as a function of strain rate, measured by cross-slot rheometer.

Initially there is the appearance of inflections in the streamlines due to the enhancement of elastic effect (see Fig. 7a). At $t = 0.25$ s, a bistable asymmetric lip vortex appears (see Fig. 7b), followed by symmetric lip vortices (see Fig. 7c) and lip vortex growth (see Fig. 7d). After sufficient time, the lip vortex grows into an unstable corner vortex as shown in Fig. 7e, and the vortex spreads toward the stagnant corner. Finally the radial location of the vortex centre

Fig. 6. Rheometric measurements of PEO aqueous solutions at 25 °C. (a) Storage modulus G' (solid symbol) and loss modulus G'' measured by PAV for $c = 0.3$ wt.% PEO solution; (b) steady shear viscosities for $c = 0.3$, 0.35, 0.4 and 0.45 wt.% PEO solutions.

saturates and the large elastic corner vortex appears and starts to grow upstream, as illustrated in Fig. 7e and f. A similar sequence of vortex evolution was also found for the other three PEO(I) solutions with $c = 0.35$, 0.4 and 0.45 wt.%. The flow pattern of the semi-dilute PEO(I) solutions in planar 8:1 contraction flow evolves from the bending streamlines to the lip vortex, then into the corner vortex flow regime. Lip vortex formation is a precursor to vortex enhancement growth.

3.4. Effect of El on vortex stability

Figs. 8 and 9 show examples of the flow pattern in 0.3 wt.% and 0.45 wt.% PEO(I) solutions at similar Wi but different El, within the lip and corner vortex flow regimes, respectively. The images were captured sequentially after the pressure drop had reached steady state.

The images in the left-hand column ($c = 0.3$ wt.%, $El = 20$) in Fig. 8 show that the lip vortex is asymmetric and bistable. The vortex position periodically switches between the left and right side of the contraction throat. The images in the right-hand column ($c = 0.45$ wt.%, $El = 120$) in Fig. 8 show that the lip vortex is symmetric and stable. The lip vortex is much more stable in higher El flow. Fig. 9 displays the streamline evolution of the same PEO(I) solutions in the corner vortex regime in higher Re and Wi flow. At $El = 20$ the inertial effects are relatively strong; both vortex structure and size are time-dependent. The flow is unsteady with the vortex not only switching from left to right but also moving up and down. When elastic effects dominate at $El = 120$, the structure of the corner vortex is nearly symmetric. The dynamical evolutions of all these vortices are 3D in nature. Fig. 10 shows the streamline evolution of 0.45 wt.% PEO(I) solution ($El = 120$) at $Q = 4$ml/h, $Re = 0.58$, $Wi = 71$ and at $Q = 5$ml/h, $Re = 0.83$, $Wi = 101$, in the left and right-hand columns, respectively. In such a high Wi flow regime, the streamlines in the vortex region are less closed and lead to dramatic 3D flow. This chaotic-like flow phenomenon results from the dominating elastic effects. Further quantitative analysis is required to determine whether the flow is truly turbulent or not.

3.5. Summary of flow regimes in Wi–Re diagram

The non-linear dynamics of all four semi-dilute PEO(I) solutions with $El = 20$, 38, 71, and 120 in planar microfluidic geometry with an 8:1:8 contraction–expansion can be characterized by a number of flow regimes summarized in a Wi–Re diagram, as suggested by Rodd et al [9]. These are illustrated in Fig. 11.

All the PEO(I) solutions at low flow rates ($Wi < 16$) exhibit pseudo-Newtonian fluid behaviour. Increasing Wi, the streamlines show bending close to the contraction throat region. The onset of elastic instability occurs close to the throat. The transition from bending streamlines to lip vortex formation is at $Wi \sim 30$. Lip vortices occur at all El numbers within a narrow window of Wi ($28 < Wi < 32$). As shown in Fig. 9, the lip vortex for low El flow is unstable and asymmetric, whereas for high El flow the lip vortex is stable and symmetric. With a slight increase of Wi, the lip vortex quickly develops into an unstable corner vortex. The corner vortex grows substantially in size and strength as Wi is increased. Once $Wi > 40$, diverging flow is observed for all the solutions. At even higher Wi, the evolution of the vortex becomes pseudo-chaotic as displayed in Fig. 11, in particular for $El = 71$ and 120.

These characteristics of vortex dynamics are different from those observed by Rodd et al. [9], using the larger contraction–expansion ratio 16:1:16, as well as the results of Gulati et al. [14], for flow of DNA solutions through a 2:1 contraction with high El ($\sim 10^4$). Gulati et al. [14] observed very symmetric and stable vortices over a wide Wi range ($4.2 < Wi < 209.6$). In comparison
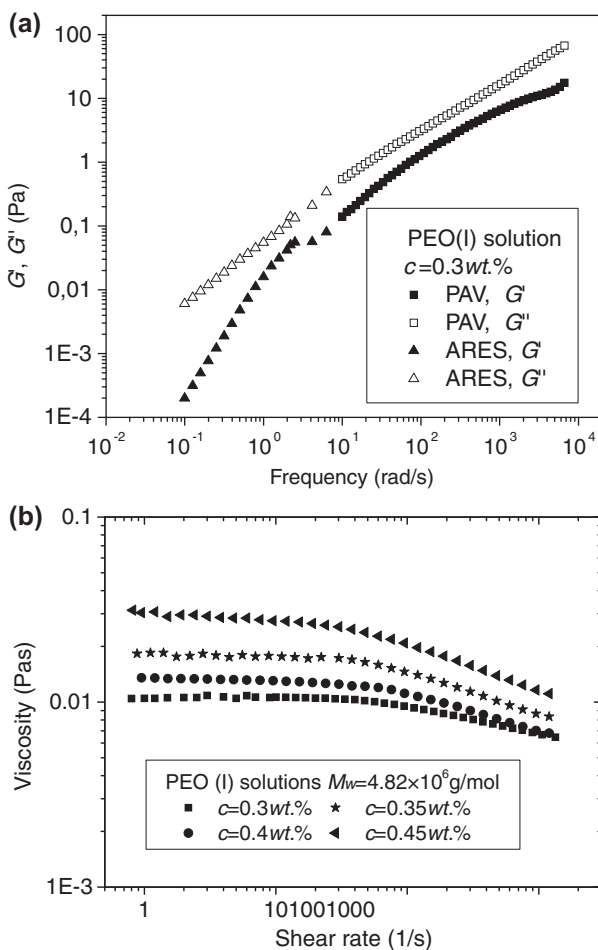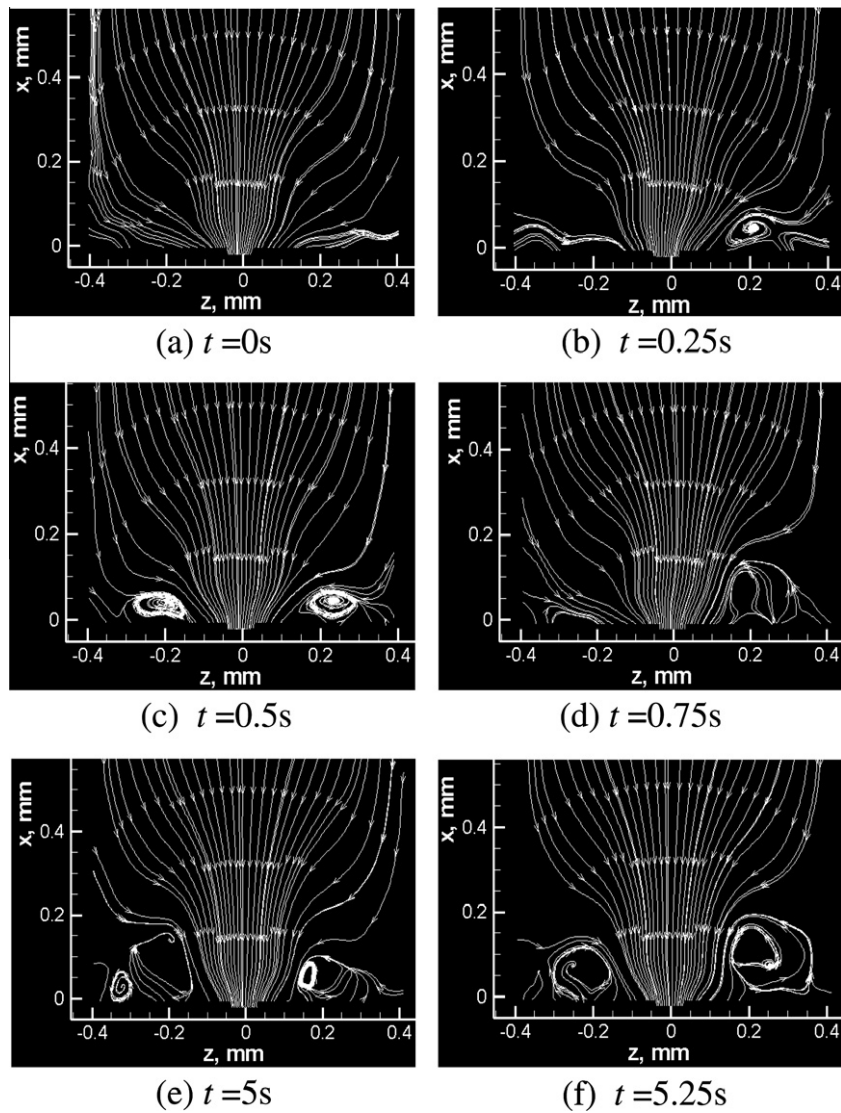
Fig. 7. Transient streamlines captured by μ-PIV for 0.3 wt.% PEO(I) solution after a step change of the flow rate from Re = 1.25, Wi = 24.9 to Re = 1.6, Wi = 32.0.

with the Wi–Re diagram of Rodd et al. [9], the onset of elastic instability in this work occurs at a lower flow rate, $Wi_{crit} \sim 30$ (compared to $Wi_{crit} \sim 50$ reported by Rodd et al). Also, in contrast to Rodd et al. [9], our results show symmetric lip vortex and symmetric corner vortex growth along the high El lines ($El > 70$). Different contraction ratios play important roles in vortex dynamics as the contraction ratio determines the Hencky strain imposed on the fluids. Moreover, the aspect ratios of the upstream flow geometries studied in literature are different: 10/11 in Gulati et al., 1/8 in Rodd et al. and 9/160 in the present work. This leads to different 3D flows, as shown by recent 3D simulation results [46]. The very long length of the narrow channel L_c in the flow geometry studied here ensures that the vortex dynamics in the upstream entry region are very loosely coupled with the fluid dynamics in the expansion region. Our results show that the vortex dynamics in this benchmark flow problem are sensitive to the details of the flow geometry, and cannot be *completely* defined by El, Re and Wi using a single geometric length scale.

3.6. Evolution of vortex size

Following the convention adopted in [47], the dimensionless vortex size is defined as $\chi_L = L_v/w_u$, where L_v is the distance

between the detachment point of the salient corner vortex and the concave corner. Evolution of vortex size is quantified by plotting the dimensionless vortex size as a function of Wi in Fig. 12. Similar to a Newtonian fluid, there is a very small vortex at the entry contraction in the low Wi flow regime. The lip vortex occurs at $Wi \sim 30$ and is maintained over a narrow window of flow rate. As it grows outward, the reattachment length remains quite small. As shown in Fig. 7 further increasing flow rate into the corner vortex regime results in a substantial increase in the vortex size. There is a nearly linear relationship between the vortex size and flow rate. This is consistent with the results of previous experimental studies with macroscale [21,22] and microscale [14] contractions. Large error bars are found for $Wi > 30$, which result from the unsteady vortex dynamics in this highly non-linear flow, as described in Sections 3.4 and 3.5.

3.7. Centreline velocity profile and evaluation of local extensional rate

Although the flow of PEO(I) solutions is in general unstable and time-dependent, for most of the cases studied here the maximum sideways displacement of the fluid core from the centreline ($y = 0$, $z = 0$) is less than 25% of w_c, and the streamline bunch close to the flow axis is nearly symmetric. The profile of extensional rate can be
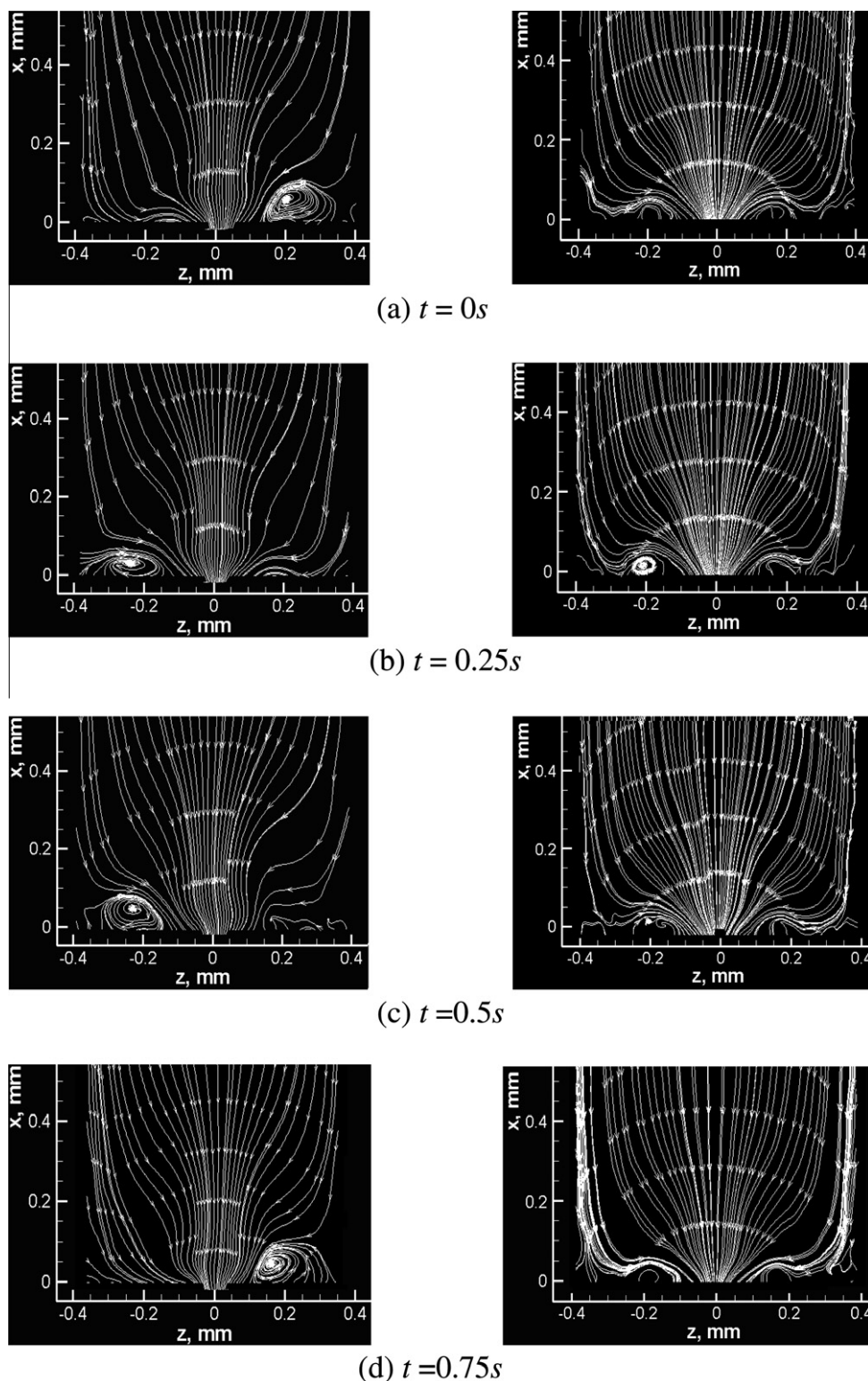
(a) $t = 0s$

(b) $t = 0.25s$

(c) $t = 0.5s$

(d) $t = 0.75s$

Fig. 8. Streamline evolution in the lip vortex flow regime captured by μ-PIV at (a) $t = 0s$, (b) $t = 0.25s$, (c) $t = 0.5$ s and (d) $t = 0.75$ s. The images of the left column are for 0.3 wt.% PEO(I) at $Q = 4.0$ ml/h, $Re = 1.4$, $Wi = 28.5$, $El = 20$, and the images of the right column are for 0.45 wt.% PEO(I) solution at $Q = 1.5$ ml/h, $Re = 0.25$, $Wi = 30.3$, $El = 120$.

readily calculated from the centreline velocity to reveal the deformation history undergone by PEO molecules flowing along the centreline and to provide some physical insight to the nonlinear fluid dynamics.

The centreline velocity profile in the upstream and downstream narrow channel was measured using a 20× objective lens ($NA = 0.45$). Due to the limitation of the view area and the very different flow speed before and after the contraction entry, the velocity fields in the upstream and downstream narrow channel were captured separately. For water, the ensemble average was taken over a sequence of 30 pairs of images. For PEO(I) solutions, the data was extracted from an instantaneous velocity field after the
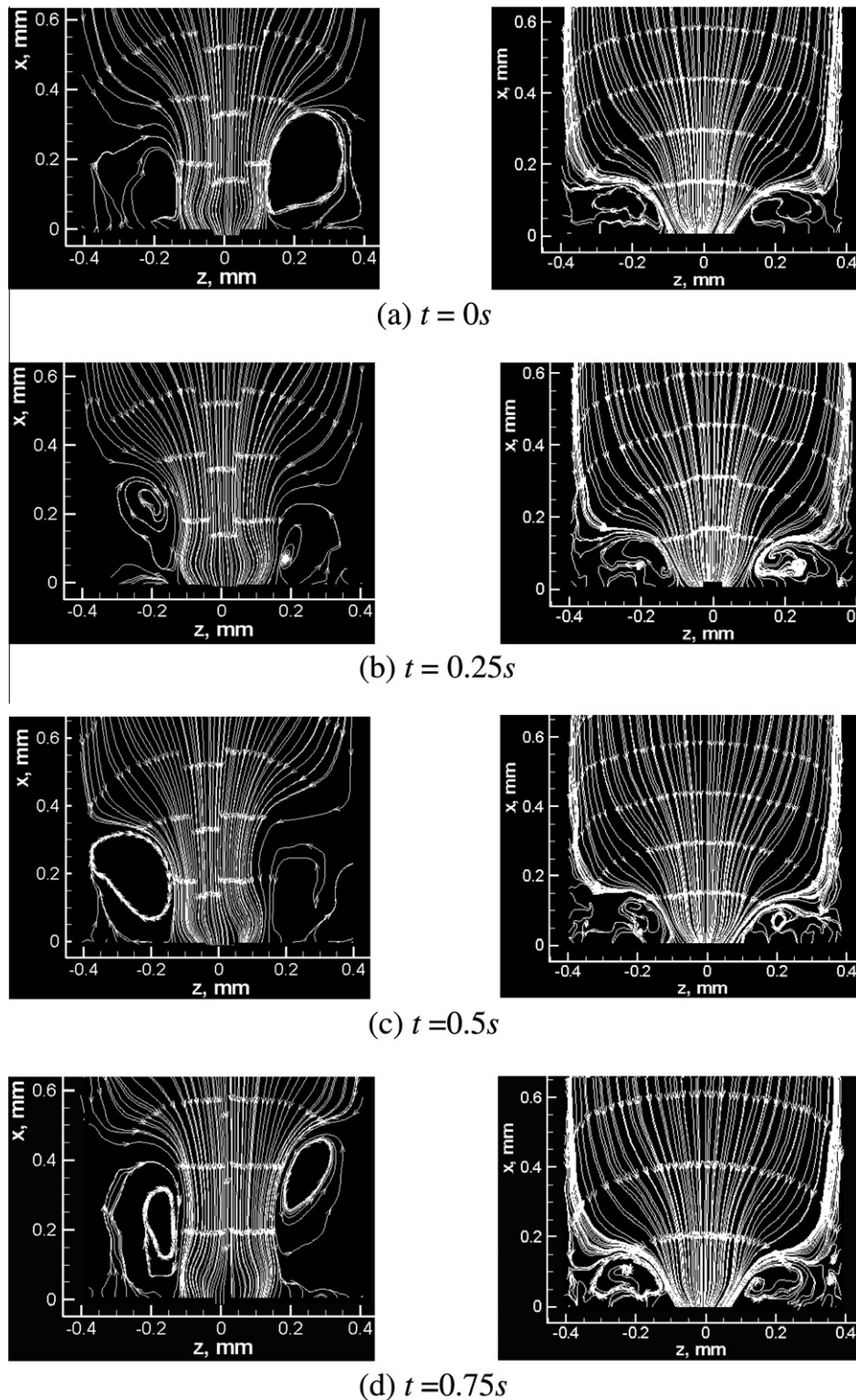
(a) $t = 0s$

(b) $t = 0.25s$

(c) $t = 0.5s$

(d) $t = 0.75s$

Fig. 9. Streamline evolution in the corner vortex flow regime captured by μ-PIV at (a) $t = 0$ s, (b) $t = 0.25$ s, (c) $t = 0.5$ s and (d) $t = 0.75$ s. The images of the left column are for 0.3 wt.% PEO(I) at $Q = 6$ml/h, $Re = 2.1$, $Wi = 42.7$, $El = 20$, and the images of the right column are for 0.45 wt.% PEO(I) solution at $Q = 2$ml/h, $Re = 0.3$, $Wi = 40.3$, $El = 120$.

pressure drop had reached steady state. All velocities were normalized by the average flow speed in the narrow channel, i.e. $\langle V_c \rangle = Q/(w_c \cdot h)$.

Figs. 13a and 14a show the dimensionless axial velocity profiles of 0.3 wt.% and 0.4 wt.% PEO(I) solution along the centreline at various flow rates ranging from 2 to 10 ml/h, along with the results of

a Newtonian fluid. Upstream, the axial velocity curve at $Wi = 14.2$ is close to the result of the Newtonian fluid. At about $Wi = 21.4$, the fluid departs from Newtonian fluid behaviour and the region of fluid acceleration extends towards the upstream area. The flow is still in the steady viscoelastic flow regime as shown in the Wi–Re diagram in Fig. 11. At about $Wi = 28.5$, the corner vortex occurs
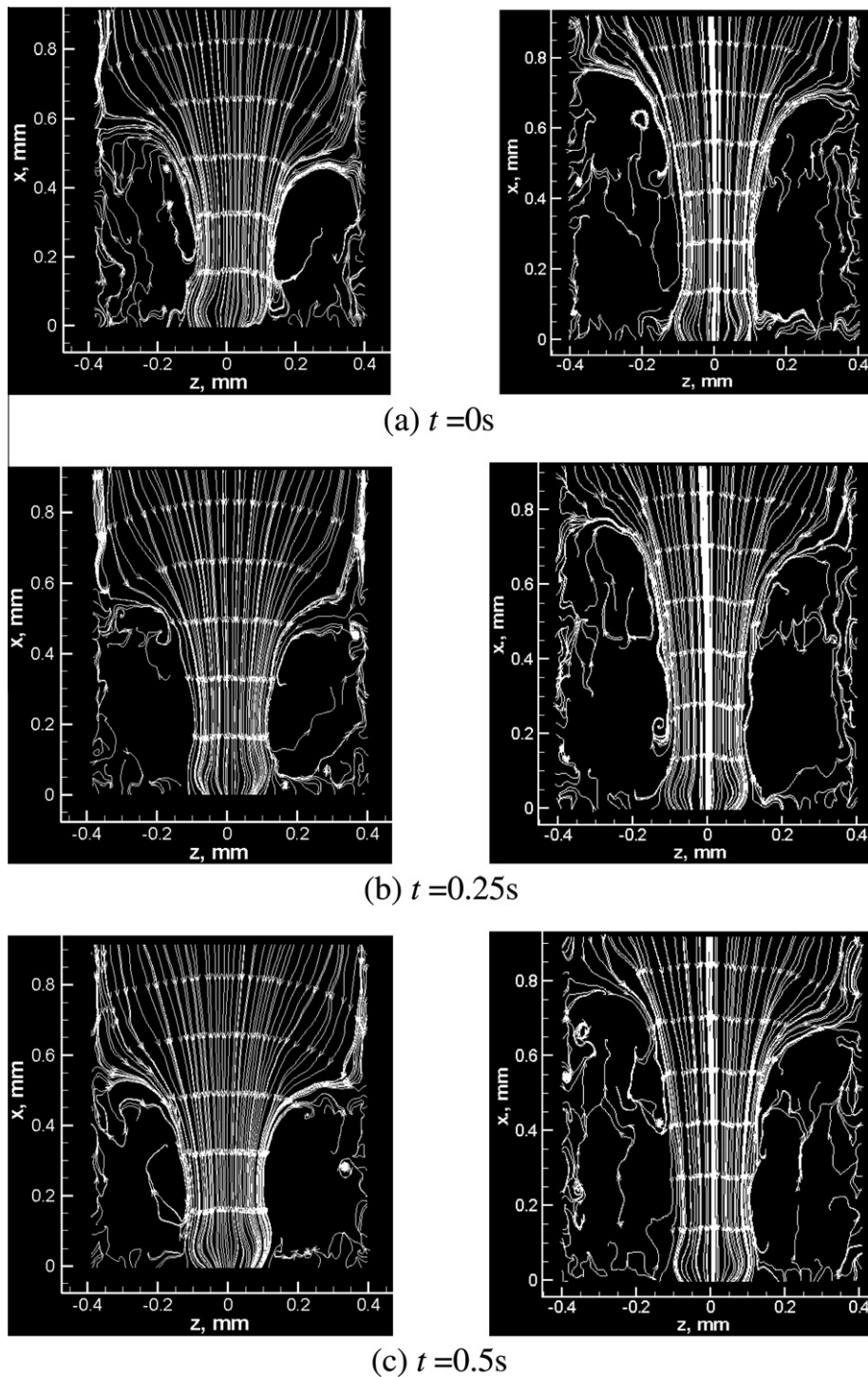
(a) $t =$ 0s

(b) $t =$ 0.25s

(c) $t =$ 0.5s

Fig. 10. The flow pattern of 0.45 wt.% PEO(I) solution in high Wi number flow regime at (a) $t = 0$ s, (b) $t = 0.25$ s and (c) $t = 0.5$ s. The left-hand column is for $Q = 4$ ml/h, $Re = 0.58$, $Wi = 71$ and the right-hand column is for $Q = 5$ ml/h, $Re = 0.83$, $Wi = 101$.

as illustrated in Fig. 12. The axial velocity profile exhibits a minimum at a position around $x/w_c = 0.8$ and this position moves upstream as the flow rate increases.

Figs. 13a and 14a also show the dimensionless axial velocity profiles in the narrow channel. Unlike the Newtonian fluid, the velocity profiles of PEO(I) solutions at low flow rates exhibit a peak. This reflects a transition from extensional to shear dominated flow, within which polymer chain re-coils after undergoing nearly pure extensional flow at the entry region. The length of this flow transition region is greatly less than the length of the narrow channel in the present work. The long narrow channel allows the flow to become fully developed and essentially acts as a buffer zone between the upstream contraction flow zone and the downstream expansion flow zone to minimize their transient interactions. Further increase of flow rate to the corner vortex regime, the velocity profile in the narrow channel tends to flatten like the Newtonian fluid. The formation of the corner vortex effectively extends the narrow channel towards the upstream. Hence the region of extensional flow shifts away from the geometric entry zone. Such a change of flow pattern actually smoothes out the peak of the velocity profile in the narrow channel.
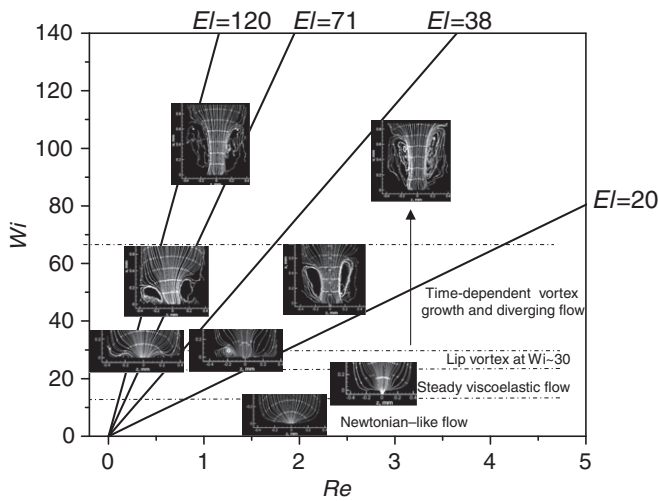
Fig. 11. Summary of flow regimes in *Wi*–*Re* diagram for four semi-dilute aqueous PEO(I) solutions through micro-fabricated contraction–expansion geometry.
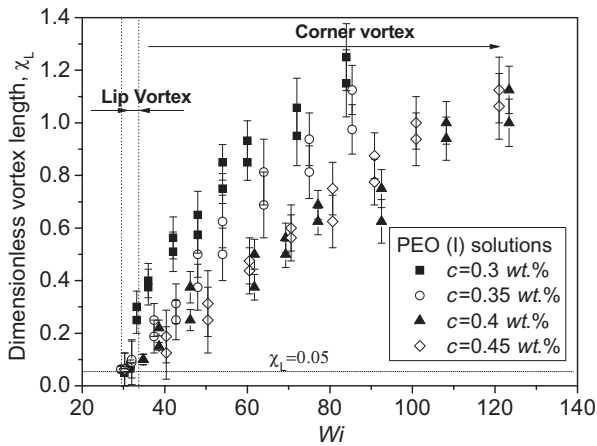

Fig. 12. Upstream dimensionless vortex lengths plotted against Weissenberg number for PEO(I) solutions flow in the 8:1:8 planar contraction–expansion.

The profile of the extensional rate along the centreline can be calculated from the corresponding velocity profile as shown in Figs. 13b and 14b. The results of 0.3 wt.% and 0.4 wt.% PEO solutions are qualitatively similar. At low flow rate ($Q \leqslant 3$ml/h), the negative sign of the extensional rates within the narrow channel indicates a long transient flow region involving compression of polymer chain after extensional deformation at the entry region. In the upstream flow, the PEO fluids start to significantly depart from Newtonian fluid behaviour when $Wi > 20$. Further increasing flow rate, the lip vortex and corner vortex regimes eventually occur. These non-linear flow phenomena couple with the appearance of a compression valley and an extensional peak in the extensional rate profile. The position of the valley and the peak shift toward the upstream area as flow rate is increased. PEO chains are first subjected to compression and then to strong extensional deformation.

3.8. Extraction of the excess pressure drop

The mean steady state pressure differences ΔP_{12} (as defined in Fig. 2) between the upstream pressure P_1 and the downstream pressure P_2 at the points 1 and 2, respectively, are plotted against *Re* or *Wi* for water and PEO solutions in Fig. 15a and b. In comparison with the results of water, the pressure drops for PEO(I)
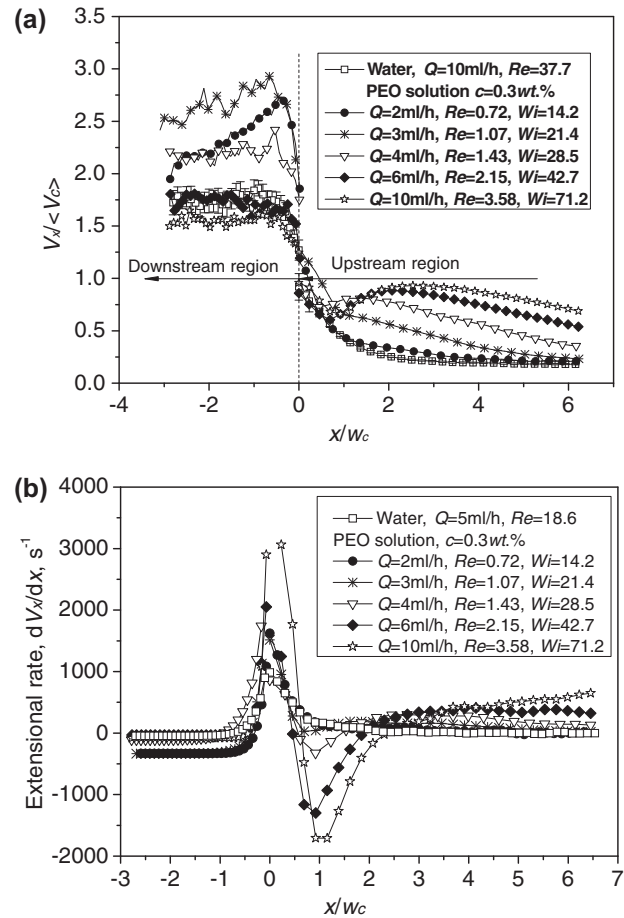

Fig. 13. 0.3 wt.% PEO(I) solution flows through 8:1 planar contraction: (a) dimensionless centreline axial velocity profile and (b) the extensional deformation rate calculated from the above velocity profile.

solutions are dramatically enhanced as *Re* or *Wi* is increased. The higher the concentration of the PEO solution, the larger is the slope of the corresponding pressure drop curve.

The excess pressure drop is defined as $\Delta P_{ex} = \Delta P_{12} - \Delta P_{FD}$, where $\Delta P_{FD} = \Delta P_{13} + \Delta P_{34} + \Delta P_{42}$, is the sum of the pressure drops as if the flow in the all three sections (see Fig. 16) is fully developed and laminar. The value of ΔP_{34} under various *Re* or *Wi* was obtained by direct measurement of the pressure drop over the 20 mm middle section of a 40 mm long microchannel, with the same cross-section as the narrow channel of the contraction–expansion flow geometry. Thus, the effect of shear-thinning in the PEO(I) solutions under high *Wi* flow has been fully accounted for. The values of $(\Delta P_{13} + \Delta P_{42})$ were calculated by $Wi \cdot d(\Delta P_{12} - \Delta P_{34})/dWi$, where the gradient $d(\Delta P_{12} - \Delta P_{34})/dWi$ was obtained by fitting the pressure curve $(\Delta P_{12} - \Delta P_{34})$ vs. *Wi* in the low *Wi* flow regime. It has been verified that the pressure drop of the Newtonian fluid is increased nearly linearly with *Re* over the range of *Re* < 40. In such low *Re* flows, the inertial contributions to the excess pressure drop are still much smaller than the contribution from the polymer viscoelasticity. Hence the excess pressure drop studied here can be used as a sensitive measure of the effect of nonlinear extensional viscosity in the contraction–expansion flow as long as *Re* is kept reasonably small.

The dimensionless pressure drop $\Delta P' = (\Delta P_{12} - \Delta P_{34} - \Delta P_{13} - \Delta P_{42})/(\Delta P_{13} + \Delta P_{42})$ is plotted against *Wi* in Fig. 16. Three regimes are clearly identified. In regime (I) (*Wi* < 30) where the fluid flow transforms from the Newtonian-like, to steady viscoelastic and then to lip vortex, there is a weak dependence of $\Delta P'$ on *Wi*. In regime (II)
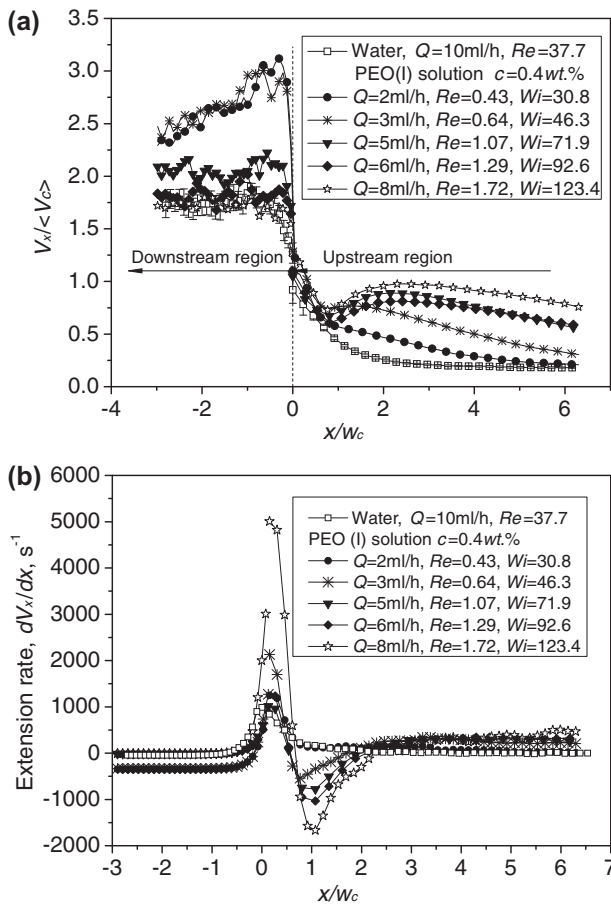
Fig. 14. 0.4 wt.% PEO(I) solution flows through 8:1 planar contraction: (a) dimensionless centreline axial velocity profile and (b) the extensional deformation rate calculated from the above velocity profile.

Fig. 15. Pressure drop vs. (a) *Re* and (b) *Wi* for PEO(I) solutions flowing through the 8:1:8 planar contraction–expansion microfluidic geometry.

$(30 < Wi < 60)$, in which the flow structure develops into corner vortex enhancement, $\Delta P'$ increases rapidly with *Wi* and reaches a maximum. After that, $\Delta P'$ decreases as *Wi* increases, probably due to the finite limit on the overall strain that can be imposed on polymer molecules through such a contraction–expansion flow. This results in the apparent extensional viscosity, η_E, starting to decrease in the high *Wi* flow regime. The shape of the $\Delta P'$ vs. *Wi* curve is similar to that reported in Rodd et al. [9]. However in the present work, $\Delta P'$ increases with the concentration of PEO(I) in the semi-dilute region studied ($c/c^* \geqslant 15$). The higher the concentration of the semi-dilute PEO solution, the smaller the polymer segment-segment correlation length is. The stronger interactions between polymer chains results in higher viscosity under flow conditions.

4. Conclusions

We have undertaken an integrated approach, including quantitative molecular characterization, rheometric and flow characterization, to study the non-linear dynamics of semi-dilute polymer solutions through micro-fabricated planar abrupt 8:1:8 contraction–expansion flow over a wide range of Elasticity numbers ($20 \leqslant El \leqslant 120$), Weissenberg numbers ($7 \leqslant Wi \leqslant 121$) and Reynolds numbers ($0.08 \leqslant Re \leqslant 4.5$). The elastic behaviour of semi-dilute PEO solutions are very sensitive to their molecular weight distribution. Semi-dilute PEO(II) solutions (with $M_w = 1.34 \times 10^6$ g/mol and $M_w/M_n = 2.82$) do not show significant elastic fluid characteristics, even at concentrations as high as $c/c^* = 22.3$ or 1.2 wt.%. PEO(I) solutions with higher polydispersity ($M_w = 4.82 \times 10^6$ g/mol
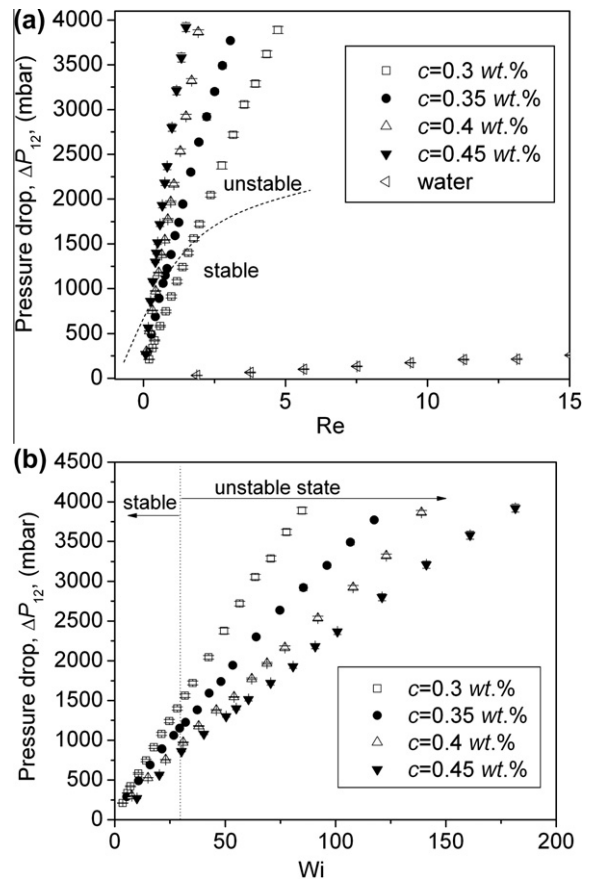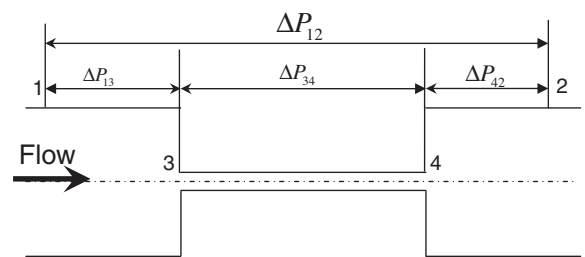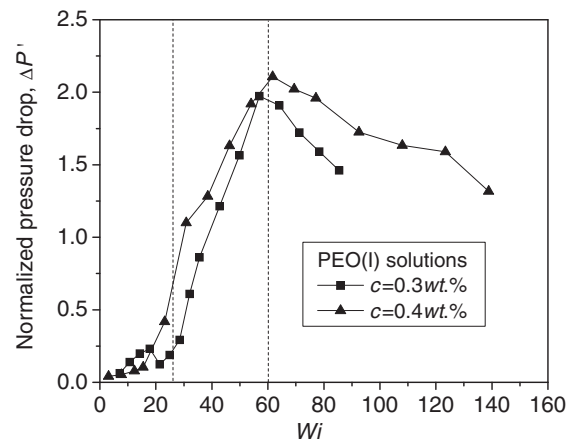

Fig. 16. Dimensionless pressure drop against *Wi* number for PEO(I) solutions flowing through an 8:1:8 planar contraction–expansion microfluidic geometry, where $\Delta P' = (\Delta P_{12} - \Delta P_{34} - \Delta P_{13} - \Delta P_{42})/(\Delta P_{13} + \Delta P_{42})$.

and M_w/M_n = 7.50) exhibit the pronounced characteristics of elastic fluids at relatively low concentration (c/c^* = 15). This shows that the rheological and flow properties of semi-dilute polymer solutions are very sensitive to the existence of the extremely long molecules in the long tail of highly polydisperse polymers.

The rheometric characterization of four semi-dilute PEO(I) solutions has been carried out using ARES rotational rheometer, a Piezo-Axial-Vibrator, CaBER and a cross-slot extensional rheometer. The relaxation spectrum can be extracted from G' and G'' data over a wide frequency range reaching up to 6300 Hz. The material functions of individual PEO(I) solutions can be readily extracted from these rheometric data gathered using these methods.

Flow characterizations of four semi-dilute PEO(I) solutions (with elasticity number, El = 16, 38, 71 and 120) through the micro-fabricated planar abrupt 8:1:8 contraction–expansion flow geometry have been carried out using μ-PIV technique and pressure drop measurement. The evolution of vortex formation and dynamics has been visualized through a step-flow-rate experiment from the lip vortex flow regime to the corner vortex flow regime. The effect of El on vortex stability has been studied. Various regimes of flow dynamics were identified and have been presented in a Wi–Re diagram. As discussed in Section 3.5, the characteristics of vortex dynamics in 8:1 contraction flow are qualitatively different from those seen by Gulati et al. [14] with a 2:1 contraction flow and by Rodd et al. [9,10] with a 16:1:16 contraction–expansion flow. Therefore the characteristics of the flow geometry, such as the contraction ratio and aspect ratio, are sensitive design parameters in controlling the non-linear dynamics of semi-dilute polymer solutions in microfluidics, which cannot be *completely* described by the dimensionless numbers, El, Wi and Re using a single geometric length scale. Quantitative experimental results from molecular characterization to rheometric and flow characterization over a wide range of flow conditions are still much needed not only to better understanding the nonlinear fluid dynamics of semi-dilute polymer solutions, but also to rigorously evaluate constitutive models and numerical codes, hence to map out a blueprint for microfluidic design.

Acknowledgements

References

[1] D.F. James, J.H. Saringer, Flow of dilute polymer solutions through converging channels, J. Non-Newtonian Fluid Mech. 11 (1982) 317–339.
[2] A. Groisman, M. Enzelberger, S.R. Quake, Microfluidic memory and control devices, Science 300 (2003) 955–958.
[3] D.E. Smith, S. Chu, Response of flexible polymers to a sudden elongational flow, Science 281 (5381) (1998) 1335–1340.
[4] J.S. Hur, E.S.G. Shaqfeh, H.P. Babcock, D.E. Smith, S. Chu, Dynamics of dilute and semidilute DNA solutions in the start-up of shear flow, J. Rheol. 45 (2001) 421–450.
[5] C.M. Schroeder, R. Teixeira, E.S.G. Shaqfeh, S. Chu, Dynamics of DNA in the flow-gradient plane of steady shear flow: observations and simulations, Macromolecules 38 (5) (2005) 1967–1978.
[6] T.T. Perkins, D.E. Smith, S. Chu, Single polymer dynamics in an elongational flow, Science 276 (1997) 2016–2021.
[7] C.M. Schroeder, H.P. Babcock, E.S.G. Shaqfeh, S. Chu, Observation of polymer conformation hysteresis in extensional flow, Science 301 (5639) (2003) 1515–1519.
[8] J.S. Hur, E.S.G. Shaqfeh, H.P. Babcock, S. Chu, Dynamics and configurational fluctuations of single DNA molecules in linear mixed flows, Phys. Rev. E 66 (011915) (2002) 1–4.
[9] L.E. Rodd, T.P. Scott, D.V. Boger, J.J. Cooper-White, G.H. Mckinley, The inertio-elastic planar entry flow of low-viscosity elastic fluids in micro-fabricated geometries, J. Non-Newtonian Fluid Mech. 129 (2005) 1–22.
[10] L.E. Rodd, J.J. Cooper-White, D.V. Boger, G.H. Mckinley, Role of the elasticity number in the entry flow of dilute polymer solutions in micro-fabricated contraction geometries, J. Non-Newtonian Fluid Mech. 143 (2007) 170–191.
[11] D. Erickson, F. Lu, D. Li, T. White, J. Gao, An experimental investigation into the dimension-sensitive viscosity of polymer containing lubricant oils in microchannels, Exp. Thermal Fluid Sci. 25 (2002) 623–630.
[12] K. Kang, L.J. Lee, K.W. Koelling, High shear microfluidics and its application in rheological measurement, Exp. Fluids 38 (2) (2005) 222–232.
[13] C.J. Pipe, T.S. Majmudar, G.H. McKinley, High shear rate viscometry, Rheol. Acta 47 (2008) 621–642.
[14] S. Gulati, S.J. Muller, D. Liepmann, Direct measurements of viscoelastic flows of DNA in a 2:1 abrupt planar micro-contraction, J. Non-Newtonian Fluid Mech. 155 (2008) 51–56.
[15] S.J. Haward, Z. Li, D. Lighter, B. Thomas, J.A. Odell, X.F. Yuan, Flow of dilute to semi-dilute polystyrene solutions through a benchmark 8:1 planar abrupt micro-contraction, J. Non-Newtonian Fluid Mech. 165 (2010) 1654–1669.
[16] P.J. Cable, D.V. Boger, Comprehensive experimental investigation of tubular entry flow of viscoelastic fluids. 1. Vortex characteristics in stable flow, AIChE J. 24 (1978) 869–879.
[17] P.J. Cable, D.V. Boger, Comprehensive experimental investigation of tubular entry flow of viscoelastic fluids. 2. Velocity-field in stable flow, AIChE J. 24 (1978) 992–999.
[18] P.J. Cable, D.V. Boger, Comprehensive experimental investigation of tubular entry flow of viscoelastic fluids. 3. Unstable flow, AIChE J. 25 (1979) 152–159.
[19] J.M. Maia, D. Binding, Influence of elongational properties on the contraction flow of polyisobutylene in a mixed solvent, Rheol. Acta 38 (1999) 160–171.
[20] J.P. Rothstein, G.H. McKinley, Extensional flow of a polystyrene Boger fluid through a 4:1:4 axisymmetric contraction/expansion, J. Non-Newtonian Fluid Mech. 86 (1999) 61–88.
[21] J.P. Rothstein, G.H. McKinley, The axisymmetric contraction–expansion: the role of extensional rheology on vortex growth dynamics and the enhanced pressure drop, J. Non-Newtonian Fluid Mech. 98 (2001) 33–63.
[22] R.E. Evans, K. Walters, Flow characteristics associated with abrupt changes in geometry in the case of highly elastic liquids, J. Non-Newton. Fluid Mech. 20 (1986) 11–29.
[23] R.E. Evans, K. Walters, Further remarks on the lip-vortex mechanism of vortex enhancement in planar-contraction flows, J. Non-Newtonian Fluid Mech. 32 (1989) 95–105.
[24] K. Chiba, T. Sakatani, K. Nakamura, Anomalous flow patterns in viscoelastic entry flow through a planar contraction, J. Non-Newtonian Fluid Mech. 36 (1990) 193–203.
[25] K. Chiba, S. Tanaka, K. Nakamura, The structure of anomalous entry flow patterns through a planar contraction, J. Non-Newtonian Fluid Mech. 42 (3) (1992) 315–322.
[26] S. Nigen, K. Walters, Viscoelastic contractions flows: comparison of axisymmetric and planar configurations, J. Non-Newtonian Fluid Mech. 102 (2002) 343–359.
[27] M. Aboubacar, H. Matallah, M.F. Webster, Highly elastic solutions for Oldroyd-B and Phan-Thien/Tanner fluids with a finite volume/element method: planar contraction flows, J. Non-Newtonian Fluid Mech. 103 (1) (2002) 65–103.
[28] M.A. Alves, P.J. Oliveira, F.T. Pinho, Benchmark solutions for the flow of Oldroyd-B and PTT fluids in planar contractions, J. Non-Newtonian Fluid Mech. 110 (1) (2003) 45–75.
[29] B. Purnode, M.J. Crochet, Flows of polymer solutions through contractions. Part 1: flows of polyacrylamide solutions through planar contractions, J. Non-Newtonian Fluid Mech. 65 (1996) 269–289.
[30] M.A. Alves, P.J. Oliveira, F.T. Pinho, On the effect of contraction ratio in viscoelastic flow through abrupt contractions, J. Non-Newtonian Fluid Mech. 122 (2004) 117–130.
[31] A. Baloch, P. Townsend, M.F. Webster, On vortex development in viscoelastic expansion and contraction flows, J. Non-Newtonian Fluid Mech. 65 (2/3) (1996) 133–149.
[32] S.C. Xue, N. Phan-Thien, R.I. Tanner, Three dimensional numerical simulations of viscoelastic flows through planar contractions, J. Non-Newtonian Fluid Mech. 74 (1–3) (1998) 195–245.
[33] S.A. White, A.D. Gotsis, D.G. Baird, Review of the entry flow problem: experimental and numerical, J. Non-Newtonian Fluid Mech. 24 (2) (1987) 121–160.
[34] M.A. Alves, F.T. Pinho, P.J. Oliveira, Visualizations of Boger fluid flows in a 4:1 square–square contraction, AIChE J. 51 (11) (2005) 2908–2922.
[35] D.M. Binding, K. Walters, On the use of flow through a contraction in estimating the extensional viscosity of mobile polymer solutions, J. Non-Newtonian Fluid Mech. 30 (1988) 233–250.
[36] P.G. de Gennes, Coil-stretch transition of dilute flexible polymers under ultrahigh velocity gradients, J. Chem. Phys. 60 (1974) 5030–5042.
[37] K. Devanand, J.C. Selser, Asymptotic behavior and long-range interactions in aqueous solutions of poly (ethylene oxide), Macromolecules 24 (1991) 5943–5947.

[38] J.J. Crassous, R. Régisser, M. Ballauff, Characterization of the viscoelastic behavior of complex fluids using the piezoelastic axial vibrator, J. Rheol. 49 (4) (2005) 851–863.

[39] J.G. Santiago, S.T. Wereley, C.D. Meinhart, D.J. Beebe, R.J. Adrian, A particle image velocimetry system for microfluidics, Exp. Fluids 25 (1998) 316–319.

[40] C.D. Meinhart, S.T. Wereley, J.G. Santiago, PIV measurements of a microchannel flow, Exp. Fluids 27 (1999) 414–419.

[41] C.D. Meinhart, S.T. Wereley, M.H.B. Gray, Volume illumination for two-dimensional particle image velocimetry, Meas. Sci. Technol. 11 (2000) 809–814.

[42] F.M. White, Viscous Fluid Flow, third ed., McGraw-Hill, New York, 2006.

[43] L.E. Rodd, T.P. Scott, J.J. Cooper-White, G.H. McKinley, Capillary break-up rheometry of low-viscosity elastic fluids, Appl. Rheol. 15 (1) (2005) 12–27.

[44] S.J. Haward, J.A. Odell, Z. Li, X.F. Yuan, The rheology of polymer solution elastic strands in extensional flow, Rheol. Acta 49 (7) (2010) 781–788.

[45] J.A. Odell, S.P. Carrington, Extensional flow oscillatory rheometry, J. Non-Newtonian Fluid Mech. 137 (1-3) (2006) 110–120.

[46] S.C. Omowunmi, X.-F. Yuan, Modelling the three-dimensional flow of a semi-dilute polymer solution in microfluidics – on the effect of aspect ratio, Rheol. Acta 49 (6) (2010) 585–595.

[47] S.A. White, D.G. Baird, Flow visualization and birefringence studies on planar entry flow behavior of polymer melts, J. Non-Newtonian Fluid Mech. 29 (1988) 245–267.